Proton-coupled electron transfer at modified electrodes by multiple pathways

Zuofeng Chen, Aaron K. Vannucci, Javier J. Concepcion, Jonah W. Jurss, and Thomas J. Meyer[1]

Department of Chemistry, University of North Carolina at Chapel Hill, Chapel Hill, NC 27599

Contributed by Thomas J. Meyer, October 20, 2011 (sent for review August 5, 2011)

In single site water or hydrocarbon oxidation catalysis with polypyridyl Ru complexes such as $[Ru^{II}(Mebimpy)(bpy)(H_2O)]^{2+}$ [where bpy is 2,2′-bipyridine, and Mebimpy is 2,6-bis(1-methylbenzimidazol-2-yl)pyridine] 2, or its surface-bound analog $[Ru^{II}(Mebimpy)(4,4'$-bis-methlylenephosphonato-2,2′-bipyridine$)(OH_2)]^{2+}$ 2-PO_3H_2, accessing the reactive states, $Ru^{V}{=}O^{3+}/Ru^{IV}{=}O^{2+}$, at the electrode interface is typically rate limiting. The higher oxidation states are accessible by proton-coupled electron transfer oxidation of aqua precursors, but access at inert electrodes is kinetically inhibited. The inhibition arises from stepwise mechanisms which impose high energy barriers for $1e^-$ intermediates. Oxidation of the Ru^{III}-OH^{2+} or Ru^{III}-$OH_2{}^{3+}$ forms of 2-PO_3H_2 to $Ru^{IV}{=}O^{2+}$ on planar fluoride-doped SnO_2 electrode and in nanostructured films of Sn(IV)-doped In_2O_3 and TiO_2 has been investigated with a focus on identifying microscopic phenomena. The results provide direct evidence for important roles for the nature of the electrode, temperature, surface coverage, added buffer base, pH, solvent, and solvent H_2O/D_2O isotope effects. In the nonaqueous solvent, propylene carbonate, there is evidence for a role for surface-bound phosphonate groups as proton acceptors.

concerted electron-proton transfer | metal oxide electrode | surface modification | electrocatalysis | spectroelectrochemistry

Electron transfer reactions involving pH-dependent proton-coupled electron transfer (PCET) couples with a change in proton content between oxidation states, such as quinone/hydroquinone (Q/H_2Q) or M=O/M-OH/M-OH_2 oxo/hydroxo/aqua transition metal couples, are often slow at inert electrodes (1–5). For these couples, the change in protonation state and the requirement to add or lose protons adds to the normal kinetic barrier to electron transfer. The PCET effect arises from the fact that oxidation or reduction at the electrode occurs by electron transfer without a change in proton content. This effect restricts interfacial mechanisms to electron transfer followed by proton transfer (ET-PT) or proton transfer followed by electron transfer (PT-ET). Both involve high-energy intermediates in nonequilibrium protonation states.

As an example, oxidation of H_2Q, $H_2Q - e^- \rightarrow H_2Q^{+\bullet}$, occurs at $E^{o\prime} = 1.10$ V vs. normal hydrogen electrode (NHE) independent of pH ($E^{o\prime}$ is the formal potential) (2). The thermodynamic potential for H_2Q oxidation at pH 7, $H_2Q - e^- - H^+ \rightarrow HQ^{\bullet}$, is $E^{o\prime} = 0.63$ V (2). An inert electrode at pH = 7 creates an overpotential of 0.47 V for the initial electron transfer in the ET-PT sequence. Following electron transfer, thermodynamic equilibrium is reached by proton loss from $H_2Q^{+\bullet}$ to the surrounding medium at the prevailing pH with $\Delta E^{o\prime} = 1.10\ \text{V} - 0.059\{\text{pH} - (\text{p}K_a(H_2Q^{+\bullet}))\}$ with $\text{p}K_a(H_2Q^{+\bullet}) = -0.95$. Oxidation can also occur by PT-ET with initial loss of a proton from H_2Q to give HQ^- followed by oxidation to $HQ^{\bullet}$ at $E^{o\prime}(HQ^{\bullet}/HQ^-) = 0.46$ V. For this mechanism, an inhibition to rate arises from the pH dependence of the electroactive anion concentration with $[HQ^-] = K_a[H_2Q]_T/([H^+] + K_a)$ and $[H_2Q]_T$ the total concentration of hydroquinone with $\text{p}K_a(H_2Q) = 9.85$ (2).

The role of PCET in electrochemical reactivity has been discussed in a series of papers (6–15). In a cyclic voltammetry (CV) study on the Os-based couples *cis*-$[Os^{IV}(bpy)_2(py)(O)]^{2+}$/*cis*-$[Os^{III}(bpy)_2(py)(OH)]^{2+}$ (where bpy is 2,2′-bipyridine) and *cis*-$[Os^{III}(bpy)_2(py)(OH)]^{2+}$/*cis*-$[Os^{II}(bpy)_2(py)(OH_2)]^{2+}$, Savéant and coworkers (7) concluded that oxidation of Os^{II}-$OH_2{}^{2+}$ to Os^{III}-OH^{2+} is dominated by ET-PT below pH 7 and by PT-ET above pH 7. The $Os^{IV} = O^{2+}/Os^{III}$-$OH^{2+}$ couple is slower than the Os^{III}-OH^{2+}/Os^{II}-$OH_2{}^{2+}$ couple by approximately 10^3 with a negligible H_2O/D_2O solvent kinetic isotope effect (KIE) in acidic solution. Rate accelerations were observed with added proton acceptor bases, the Britton–Robinson buffer (phosphate, citrate, borate, and acetate), accompanied by the appearance of a solvent KIE of 2–2.5. The latter was attributed to concerted electron-proton transfer (EPT) at the electrode with electron transfer to the electrode occurring in concert with proton transfer to the added base form of the buffer (7).

Although water as the solvent could, in principle, act as a proton acceptor or donor, its participation is limited by its acid-base properties with $\text{p}K_a(H_3O^+) = -1.74$ and $\text{p}K_a(H_2O) = 15.7$. Concerted EPT pathways involving solvent are favorable only for exceedingly strong acids or bases. Where driving forces are comparable, ET is expected to be favored over EPT due to more complex reaction barriers and slower rates for the latter (2).

Electrocatalysis by deliberate introduction of PCET pathways at modified electrode surfaces has been reported (6–15). This study is important in extending solution reactivity, for example, toward water and hydrocarbon oxidation catalysis, to electrode interfaces in device configurations.

Oxidative activation of carbon electrodes introduces surface quinoidal functional groups which activate PCET couples by enabling concerted EPT pathways at the modified surface (10). For the surface-bound analog of $[Ru^{II}(tpy)(bpy)(OH_2)]^{2+}$ (tpy is 2,2′:6′,2″-terpyridine) **1**, $[Ru^{II}(tpy)(4,4'$-$(PO_3H_2CH_2)_2$bpy$)(OH_2)]^{2+}$ ($4,4'$-$(PO_3H_2CH_2)_2$bpy is 4,4′-bis-methlylenephosphonato-2,2′-bipyridine) **1-PO_3H_2**, on planar Sn(IV)-doped In_2O_3 (ITO) electrodes, a reversible $Ru^{IV}{=}O^{2+}/Ru^{III}$-$OH^{2+}$ wave appears but only at high surface coverages (11). This observation was attributed to the surface coverage-dependent, cross-surface disproportionation mechanism in Scheme 1. For ITO|**1**–PO_3H_2, initial disproportionation on the surface occurs with $\Delta G^{o\prime} =$ 0.09 eV. Disproportionation is presumably followed by the ET-PT sequence ITO-Ru^{II}-$OH_2{}^{2+} - e^- \rightarrow$ ITO-Ru^{III}-$OH_2{}^{3+}$; ITO-Ru^{III}-$OH_2{}^{3+} - H^+ \rightarrow$ ITO-Ru^{III}-OH^{2+} with ITO-Ru^{III}-OH^{2+} reentering the disproportionation cycle (11).

PCET half reactions and EPT pathways play key roles in biological redox reactions (2, 16, 17) and, in a general way, in oxidation-reduction catalysis (2, 18–26). For example, in single site water oxidation catalysis based on polypyridyl Ru complexes such as $[Ru^{II}(Mebimpy)(bpy)(H_2O)]^{2+}$ [Mebimpy is 2,6-bis(1-methylbenzimidazol-2-yl)pyridine] **2**, or its surface-bound ana-

Author contributions: Z.C. and T.J.M. designed research; Z.C. and A.K.V. performed research; J.J.C. and J.W.J. contributed new reagents/analytic tools; Z.C., A.K.V., J.J.C., and T.J.M. analyzed data; and Z.C. and T.J.M. wrote the paper.

The authors declare no conflict of interest.

[1]To whom correspondence should be addressed. E-mail: tjmeyer@unc.edu.

See Author Summary on page 20863.

This article contains supporting information online at www.pnas.org/lookup/suppl/doi:10.1073/pnas.1115769108/-/DCSupplemental.

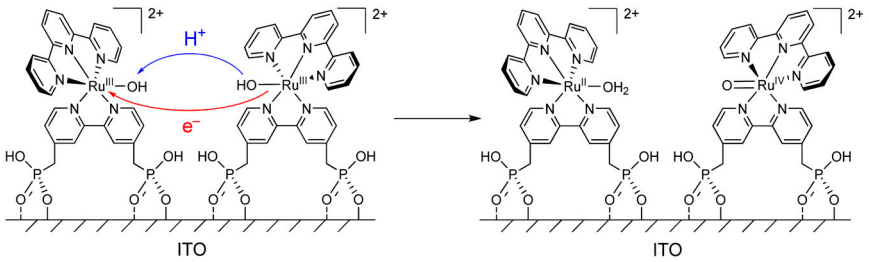

Scheme 1. Cross-surface disproportionation pathway for accessing $Ru^{IV}=O^{2+}$ at ITO|**1-PO$_3$H$_2$** at pH 1 (0.1 M $HClO_4$).

log $[Ru^{II}(Mebimpy)(4,4'\text{-}(PO_3H_2CH_2)_2bpy)(OH_2)]^{2+}$ **2-PO$_3$H$_2$** (Scheme 2), oxidative activation occurs by sequential e^-/H^+ transfer: $Ru^{II}\text{-}OH_2^{2+} - e^- - H^+ \rightarrow Ru^{III}\text{-}OH^{2+}$; $Ru^{III}\text{-}OH^{2+} - e^- - H^+ \rightarrow Ru^{IV}=O^{2+}$ (18–21). PCET oxidation to $Ru^{IV}=O^{2+}$ is followed by oxidation to $Ru^{V}=O^{3+}$ (18–21). Either or both $Ru^{IV}=O^{2+}$ and $Ru^{V}=O^{3+}$ are active as oxidation catalysts. In catalytic cycles based on these oxidants, slow oxidation of $Ru^{III}\text{-}OH^{2+}$ to $Ru^{IV}=O^{2+}$ can contribute to or even dominate rate limiting behavior in electrocatalysis or in photoelectrochemical solar fuels applications.

We report here the results of an investigation on the $Ru^{IV}=O^{2+}/Ru^{III}\text{-}OH_2^{3+}$,$Ru^{III}\text{-}OH^{2+}$ couple for surface-bound **2-PO$_3$H$_2$** on planar fluoride-doped SnO_2 (FTO), and nanostructured films of ITO (nanoITO) and TiO_2 (nanoTiO$_2$). The focus of the study was not on quantitation, but rather on uncovering microscopic phenomena associated with electrochemical interconversion of the two oxidation states. The goal of this research was to establish the mechanism by which surface oxidation and rereduction occur for the surface couple on metal oxide electrodes. Our results demonstrate the kinetic difficulties associated with this couple, identify multiple surface pathways by which it can occur, and assess the roles played by the electrode, temperature, surface coverage, added buffer base, pH, solvent, and solvent H_2O/D_2O isotope effect.

A Pourbaix ($E_{1/2}$ vs. pH) diagram for **2-PO$_3$H$_2$** on planar FTO electrodes is shown in *SI Appendix*, Fig. S1. It is slightly modified from a previous literature version (18). As a summary of the properties of the couples (22 °C), $E_{1/2}(Ru^{III/II}\text{-}OH_2^{3+/2+}) \sim E^{o\prime}(Ru^{III/II}\text{-}OH_2^{3+/2+}) = 0.82$ V; $E_{1/2}(Ru^{III/II}\text{-}OH^{2+/+}) \sim E^{o\prime}(Ru^{III/II}\text{-}OH^{2+/+}) = 0.29$ V; $pK_a(Ru^{III}\text{-}OH_2^{3+}) = 2.5$; $pK_a(Ru^{II}\text{-}OH_2^{2+}) = 11.3$; $\Delta E^{o\prime} = \sim 300$ mV for the potential difference between $Ru^{IV}=O^{2+}/Ru^{III}\text{-}OH^{2+}$ and $Ru^{III}\text{-}OH^{2+}/Ru^{II}\text{-}OH_2^{2+}$ couples (18). In addition, there is evidence for a protonated form of Ru(IV), $Ru^{IV}(OH)^{3+}$, with $pK_a \sim 3$ (26).

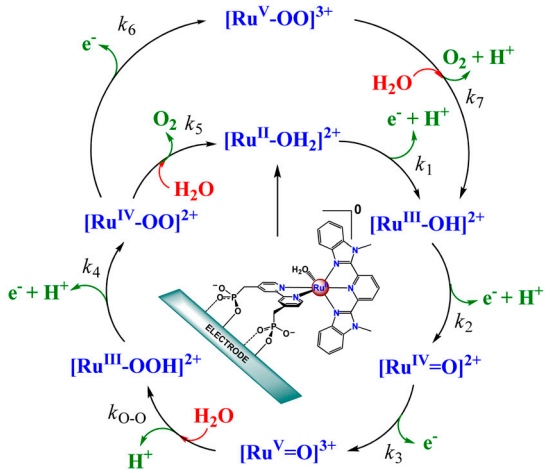

Scheme 2. Mechanism of water oxidation by **2-PO$_3$H$_2$** on metal oxide electrodes at pH 5 (17).

Results and Discussion

Surface Electrochemistry. Fig. 1 shows CVs of (*A*) FTO|**2-PO$_3$H$_2$**, (*B*) nanoITO|**2-PO$_3$H$_2$**, and (*C*) nanoTiO$_2$|**2-PO$_3$H$_2$**. All three were obtained at full surface coverages with $\Gamma/\Gamma_o = 1$ (note Table 1) at pH 5 (0.1 M HOAc/OAc$^-$) at 10 mV/s. The surface electrochemistry of the complex on planar ITO is similar to that on planar FTO and is not discussed here. CVs obtained at room temperature, 22 °C, are shown in blue and at 80 °C in red.

Nature of the electrode. At 22 °C, 1e$^-$ waves appear for the $Ru^{III}\text{-}OH^{2+}/Ru^{II}\text{-}OH_2^{2+}$ couple at $E_{1/2} = 0.68 \pm 0.01$ V with ΔE_p ($= E_{p,a} - E_{p,c}$) = 15 mV (FTO), 40 mV (nanoITO), and 105 mV (nanoTiO$_2$) at a scan rate of 10 mV/s. A pH independent $Ru^{V}=O^{3+}/Ru^{IV}=O^{2+}$ wave (not shown) appears at approximately 1.65 V, as reported earlier in a study on water oxidation (18). Potential scans to this wave trigger catalytic water oxidation with only the onset shown in Fig. 1.

At FTO and nanoITO, oxidative peak currents ($i_{p,a}$) for the Ru(II → III) oxidation wave vary linearly with scan rate (υ) as expected for a surface couple (27) (*SI Appendix*, Figs. S2 and S3). By contrast, on nanoTiO$_2$, $i_{p,a}$ varies with the square root of the scan rate ($\upsilon^{1/2}$) (*SI Appendix*, Fig. S4). A related phenomenon was reported earlier for $[Os(bpy)(4,4'\text{-}(PO_3H_2)_2bpy)]^{2+}$ surface-bound to nanoTiO$_2$ and attributed to Os(II → III) oxidation by cross-surface, diffusional electron transfer (28). In this process, site-to-site electron transfer hopping and counter ion transport occur between surface couples providing a cross-surface electron transfer channel to the underlying electrode.

CV waveforms for $Ru^{III}\text{-}OH^{2+} \rightarrow Ru^{IV} = O^{2+}$ oxidation at this pH are highly dependent on the nature of the electrode (Fig. 1). At FTO|**2-PO$_3$H$_2$** at 10 mV/s, a barely discernible wave or waves appear between 0.9 and 1.3 V (Fig. 1*A*). Reversal of the potential scan results in Ru(IV → III) rereduction at $E_{p,c} = \sim 0.83$ V. Kinetic inhibition to $Ru^{III}\text{-}OH^{2+} \rightarrow Ru^{IV}=O^{2+}$ oxidation is shown by the dependence of the current for the Ru(IV → III) rereduction wave on the time held past the Ru(III → IV) wave, either through scan rate variations (*SI Appendix*, Fig. S2) or by switching potential variations (*SI Appendix*, Fig. S5).

A dramatically different result is obtained for $Ru^{III}\text{-}OH^{2+} \rightarrow Ru^{IV}=O^{2+}$ oxidation at nanoITO|**2-PO$_3$H$_2$** (Fig. 1*B*). At a scan rate of 10 mV/s, a nearly reversible oxidative wave is observed at $E_{p,a} = 1.0$ V but of integrated current only approximately 50% of that for the Ru(III/II) wave. For the reverse, Ru(IV → III) reduction, $E_{p,c} = 0.92$ V but with a waveform that is noticeably decreased in half-width. Integrated currents for oxidative and reductive waves are comparable.

Both the current and waveform for the Ru(III → IV) wave are strongly dependent on scan rate (*SI Appendix*, Fig. S3). At 2 mV/s, Ru(III → IV) oxidation is more nearly complete and integrated currents were nearly comparable for the Ru(III → IV) and Ru(II → III) waves. At higher scan rates (50 mV/s), a new, scan-rate-dependent Ru(III → IV) wave appears at $E_{p,a} = 1.28$ V at the expense of the wave at $E_{p,a} = 1.0$ V. The new wave dominates with further increases in scan rate up to 100 mV/s. In the reverse scan, the narrow waveform for Ru(IV → III) reduction is nearly independent of scan rate but $E_{p,c}$ shifts negatively

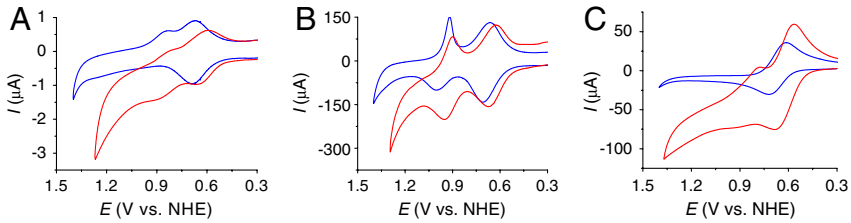

Fig. 1. CVs of (*A*) FTO|**2-PO$_3$H$_2$**, (*B*) nanoITO|**2-PO$_3$H$_2$**, and (*C*) nanoTiO$_2$|**2-PO$_3$H$_2$** with full surface coverages ($\Gamma/\Gamma_o = 1$, note Table 1) at pH 5 (0.1 M HOAc/OAc$^-$) at 22 °C (blue) and 80 °C (red). Scan rate, 10 mV/s.

with increasing scan rate. The appearance of two Ru(III → IV) oxidation waves and the narrow waveform for Ru(IV → III) reduction are notable observations and will be discussed below.

As shown in Fig. 1*C* and *SI Appendix*, Fig. S4, at nanoTiO$_2$|**2-PO$_3$H$_2$**, kinetic inhibition is complete with no evidence for a wave or waves for Ru(III → IV) oxidation over a range of scan rates. This result is consistent with the slow cross-surface, site-to-site electron transfer hopping observed for the Ru(III/II) couple.

Temperature. The three electrodes respond differently to an increase in temperature from 22 to 80 °C. At FTO|**2-PO$_3$H$_2$** the overall waveform and peak current for the kinetically facile Ru(II → III) oxidation are relatively unaffected, but the peak current for the kinetically inhibited Ru(III → IV) oxidation increases from barely discernible to becoming comparable to the peak current for the Ru(II → III) wave. A similar effect was observed on nanoITO|**2-PO$_3$H$_2$** with the Ru(II → III) wave relatively unaffected but the integrated current ratio for the Ru(III → IV) and Ru(II → III) waves increasing from approximately 50% at 22 °C to about 100% at 80 °C at 10 mV/s. At nanoTiO$_2$ the peak current for the Ru(III/II) wave at $E_{1/2} = 0.68$ V is significantly enhanced and a kinetically inhibited wave for the Ru(IV/III) couple appears at $E_{1/2} = \sim 0.9$ V. At all three electrodes, the increase in temperature from 22 to 80 °C causes an approximately −40 mV shift in $E_{1/2}$ for both couples (after accounting for the temperature dependence of the reference electrode). The negative temperature coefficients are consistent with a decrease in entropy for both couples, largely due to solvation of the released proton, e.g., Ru^{II}-$OH_2^{2+} - e^- - H^+ \rightarrow Ru^{III}$-$OH^{2+}$ (29).

Surface Loading Effects. The data in Fig. 2*A* at pH 5 (0.1 M HOAc/OAc$^-$) at 22 °C reveal a surface loading effect on the Ru(III → IV) wave at nanoITO|**2-PO$_3$H$_2$** while leaving the waveform for the Ru(III/II) couple unaffected. At low coverages, with the surface dilute in complex (green line, $\Gamma/\Gamma_o = 0.1$), a Ru(III → IV) oxidation wave appears at $E_{p,a} = \sim 1.26$ V with Ru(IV → III) rereduction occurring at $E_{p,c} = \sim 0.83$ V at 10 mV/s.

As surface loading is increased to $\Gamma/\Gamma_o = 0.25$ (blue line), the wave for Ru(III → IV) oxidation at $E_{p,a} = \sim 1.0$ V, observed on the fully loaded surface with $\Gamma/\Gamma_o = 1$ in Fig. 1, also appears but at the expense of the wave at $E_{p,a} = \sim 1.26$ V. The reverse Ru(IV → III) wave remains narrow in half-width with $E_{p,c}$ shifting to more positive potentials as surface loading is increased.

Table 1. Saturated surface coverages for 2-PO$_3$H$_2$ derivatized electrodes

Electrode	FTO|**2-PO$_3$H$_2$**	nanoITO|**2-PO$_3$H$_2$**	nanoTiO$_2$|**2-PO$_3$H$_2$**
Geometric area (cm^2)/film Thickness, μm	1.25/NA	1.25/approx 2.5	1.25/approx 10
Γ_o, mol/cm^2	1.2×10^{-10}*	1.7×10^{-8}†	5.3×10^{-8}†

*Determined from the area under the CV wave for the Ru(III/II) couple at 0.68 V vs. NHE at pH 5.

†Calculated from the film absorbance at $\lambda_{max} = 494$ nm with $\varepsilon_{max} = 1.55 \times 10^4$ M^{-1} cm^{-1} at pH 5 and the expression, $\Gamma = A(\lambda)/(10^3 \times \varepsilon(\lambda))$, with $A(\lambda)$ and $\varepsilon(\lambda)$ the absorbance and molar absorptivity at 494 nm.

The switching potential result in *SI Appendix*, Fig. S6 shows that both oxidations result in the same wave for Ru(IV → III) rereduction at $E_{p,c} = 0.92$ V at 10 mV/s. On a fully covered surface, $\Gamma/\Gamma_o = 1$ (dark-yellow line), only the Ru(III → IV) wave at $E_{p,a} = 1.0$ V is observed.

Analysis of these results points to two pathways for Ru (III → IV) oxidation:

1. At low surface coverages and high scan rates, above the pK$_a$ for nanoITO-Ru^{III}-OH_2^{3+}, direct oxidation of Ru^{III}-OH^{2+} to $Ru^{IV}(OH)^{3+}$ occurs at $E_{p,a} \sim 1.26$ V by the ET-PT mechanism in [**1**]. There is no corresponding $Ru^{IV}(OH)^{3+}/Ru^{III}$-$OH^{2+}$ rereduction wave at this pH because once $Ru^{IV}(OH)^{3+}$ is formed, it deprotonates rapidly ([**1b**]). As noted above, pK$_a \sim 3$ for the equilibrium, $Ru^{IV}(OH)^{3+} \leftrightarrow Ru^{IV}{=}O^{2+} + H^+$. There is no additional characterization data for $Ru^{IV}(OH)^{3+}$ and its structure is uncertain.

$$\text{nanoITO-}Ru^{III}\text{-}OH^{2+} - e^- \rightarrow \text{nanoITO-}Ru^{IV}(OH)^{3+}. \quad \textbf{[1a]}$$

$$\text{nanoITO-}Ru^{IV}(OH)^{3+} - H^+ \rightarrow \text{nanoITO-}Ru^{IV}{=}O^{2+}. \quad \textbf{[1b]}$$

This conclusion is reinforced by the surface coverage-independent results at pH 1 (0.1 M HNO$_3$) in Fig. 2*B*. Under these conditions, a kinetically distorted but chemically reversible Ru(IV/III) couple appears at $E_{1/2} = 1.27$ V at 10 mV/s with the Ru(III/II) couple appearing at $E_{1/2} = 0.82$ V. For the Ru (IV/III) wave, as for the Ru(III/II) wave, the current increases linearly with surface coverage with the waveform and peak potential nearly independent of surface coverage.

From the $E_{1/2}$-pH diagram in *SI Appendix*, Fig. S1, pK$_a$(Ru^{III}-OH_2^{3+}) = 2.5 for surface-bound **2-PO$_3$H$_2$**. At pH 1, the Ru (III/II) couple is Ru^{II}-$OH_2^{2+} - e^- \rightarrow Ru^{III}$-$OH_2^{3+}$, and the Ru(IV/III) couple is Ru^{III}-$OH_2^{3+} - e^- - H^+ \rightarrow Ru^{IV}(OH)^{2+}$. The electrode mechanism for Ru(III → IV) oxidation at pH 1 (0.1 M HNO$_3$) is presumably PT-ET as shown in [**2**]. In this mechanism, initial deprotonation of Ru^{III}-OH_2^{3+} is followed by electron transfer oxidation of Ru^{III}-OH^{2+} to $Ru^{IV}(OH)^{3+}$. The $Ru^{IV}(OH)^{3+}/Ru^{III}$-$OH_2^{3+}$ couple is kinetically inhibited as seen by the increase in $\Delta E_p (= E_{p,a} - E_{p,c}) = 140$ mV as compared to 25 mV for the Ru^{III}-OH_2^{3+}/Ru^{II}-OH_2^{2+} wave at 10 mV/s, perhaps indicative of a more significant structural

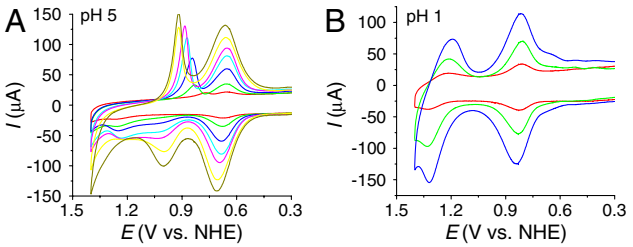

Fig. 2. CVs of nanoITO|**2-PO$_3$H$_2$** with (*A*) $\Gamma/\Gamma_o = 0.03$ (red), 0.1 (green), 0.25 (blue), 0.4 (cyan), 0.6 (magenta), 0.85 (yellow), 1 (dark yellow) at pH 5 (0.1 M HOAc/OAc$^-$), and (*B*) $\Gamma/\Gamma_o = 0.1$ (red), 0.4 (green), 1 (blue) at pH 1 (0.1 M HNO$_3$). Scan rate, 10 mV/s; temperature, 22 °C.

change between $Ru^{IV}(OH)^{3+}$ and Ru^{III}-OH^{2+} than simple proton transfer.

$$\text{nanoITO-Ru}^{III}\text{-OH}_2^{3+} - H^+ \rightarrow \text{nanoITO-Ru}^{III}\text{-OH}^{2+}. \quad \textbf{[2a]}$$

$$\text{nanoITO-Ru}^{III}\text{-OH}^{2+} - e^- \rightarrow \text{nanoITO-Ru}^{IV}(OH)^{3+}. \quad \textbf{[2b]}$$

2. Facilitation of Ru(III → IV) oxidation at high surface coverages points to higher order involvement of surface-bound sites. A reasonable origin is oxidation of Ru^{III}-OH^{2+} to $Ru^{IV}{=}O^{2+}$ by a disproportionation mechanism, [**3**], analogous to the mechanism shown in Scheme 1 (11). High loadings and close contact across the surface are required for the proton transfer part of EPT in [**3a**]. It is short range in nature due to the requirement for vibrational wave function overlap in order for proton tunneling to occur (2,30). Although there is no experimental evidence, the mediation of proton transfer by one or more water molecules may be involved.

$$2\text{nanoITO-Ru}^{III}\text{-OH}^{2+} \rightarrow \text{nanoITO-Ru}^{IV}{=}O^{2+} + \text{nanoITO-Ru}^{II}\text{-OH}_2^{2+}. \quad \textbf{[3a]}$$

$$\text{nanoITO-Ru}^{II}\text{-OH}_2^{2+} - e^- \rightarrow \text{nanoITO-Ru}^{III}\text{-OH}_2^{3+}. \quad \textbf{[3b]}$$

$$\text{nanoITO-Ru}^{III}\text{-OH}_2^{3+} - H^+ \rightarrow \text{nanoITO-Ru}^{III}\text{-OH}^{2+}. \quad \textbf{[3c]}$$

For the disproportionation step in [**3a**], $\Delta G^{o\prime} = 0.3$ eV for Ru^{III}-OH^{2+} on nanoITO|**2-PO$_3$H$_2$** at pH 5 compared to 0.09 eV for Ru^{III}-OH^{2+} of **1-PO$_3$H$_2$**. This increase contributes to the reaction barrier and decreased rate. The impact of slow kinetics is observed in the appearance of both direct oxidation and disproportionation pathways on fully loaded surfaces at relatively rapid scan rates (*SI Appendix*, Fig. S3). At these scan rates, oxidation by disproportionation at $E_{p,a} = 1.0$ V is incomplete at the thermodynamic potential for the couple. Sites that remain unoxidized during the scan undergo oxidation by direct electron transfer at the potential for the $Ru^{IV}(OH)^{3+}/Ru^{III}$-$OH^{2+}$ couple followed by proton loss to give $Ru^{IV}{=}O^{2+}$, [**1**].

Utilization of both pathways on less than fully loaded surfaces explains the simultaneous appearance of disproportionation and direct oxidation waves in Fig. 2*A*. Given the anticipated sensitivity to separation distance for disproportionation and the requirement to minimize proton tunneling distances on partly loaded surfaces, there is presumably a distribution of sites in appropriate orientations for disproportionation to occur. Oxidation of separated sites and sites with inappropriate orientations toward neighbors are limited to the direct oxidation pathway.

At high surface coverages on FTO|**2-PO$_3$H$_2$** at pH 5 (0.1 M $HOAc/OAc^-$), there is also (barely discernible) evidence for Ru(III → IV) oxidation waves at $E_{p,a} \sim 1.01$ and 1.24 V at 10 mV/s (*SI Appendix*, Fig. S7*A*). This result points to contributions to Ru(III → IV) oxidation from both direct oxidation and cross-surface disproportionation oxidation pathways, [**1**] and [**3**], on planar FTO as well. However, the effect is far more prominent in the three-dimensional nanoITO structure, suggesting a role for the three-dimensional internal cavity structure in the latter. At pH 1 (0.1 M HNO_3), as on nanoITO|**2-PO$_3$H$_2$**, kinetic inhibition of the $Ru^{IV}(OH)^{3+}/Ru^{III}$-$OH_2^{3+}$ couple was also observed with an ill-defined Ru(III → IV) wave appearing at $E_{p,a} = \sim 1.37$ V and Ru(IV → III) rereduction at $E_{p,c} = 1.15$ V (*SI Appendix*, Fig. S7*B*).

Base Effect. Significant rate accelerations for Ru(III → IV) oxidation are also observed with OAc^- added to the external solution as a proton acceptor base. As discussed below, this observation points to a third pathway for Ru^{III}-$OH^{2+} \rightarrow Ru^{IV}{=}O^{2+}$ oxidation, base-assisted, concerted EPT as reported by Savéant and coworkers in the oxidation of *cis*-$[Os^{III}(bpy)_2(py)(OH)]^{2+}$ to *cis*-$[Os^{IV}(bpy)_2(py)(O)]^{2+}$ (7). Illustrative data are shown in Fig. 3*A* for nanoITO|**2-PO$_3$H$_2$** at a surface coverage of $\Gamma/\Gamma_o = 0.35$. The base effect is present at all surface coverages but is more pronounced at low surface coverages. In these experiments, the total concentration of buffer was increased with pH held constant at pH 5 at the buffer ratio, $[OAc^-]/[HOAc] = 0.56$. Addition of $LiCF_3SO_3$ to maintain the ionic strength gave equivalent results.

The Ru(III/II) couple is largely unaffected by added buffer in this concentration range. However, increasing the concentration of OAc^- results in an increase in $i_{p,a}$ for the Ru^{III}-$OH^{2+} \rightarrow Ru^{IV}{=}O^{2+}$ wave at $E_{p,a} = 1.0$ V at the expense of $i_{p,a}$ for the Ru^{III}-$OH^{2+} \rightarrow Ru^{IV}(OH)^{3+}$ wave at $E_{p,a} = 1.26$ V. The peak current for $Ru^{IV}{=}O^{2+} \rightarrow Ru^{III}$-$OH^{2+}$ rereduction is unaffected by added buffer, but $E_{p,c}$ shifts from 0.87 to 0.92 V as $[HOAc/OAc^-]$ was increased from 0.1 to 1.0 M.

As shown in [**4**], $HOAc/OAc^-$ may play a role in catalysis of the surface-bound Ru(IV/III) couple with preassociation of OAc^- to Ru^{III}-OH^{2+} occurring by a hydrogen bond/ion-pair interaction prior to oxidation (12). The wave for Ru(IV → III) rereduction remains skewed with a narrow half-width. The shift in $E_{p,c}$ with added $HOAc/OAc^-$ at fixed scan rate is consistent with a role for prior association between $Ru^{IV}{=}O^{2+}$ and HOAc prior to reduction and the Ru(IV/III) couple, $\{Ru^{IV}{=}O^{2+}\cdots HOAc\}^{2+}/\{Ru^{III}\text{-}OH^{2+}\cdots OAc^-\}^+$ at $E_{1/2} = 0.96$ V at pH 5 at 10 mV/s.

$$\text{nanoITO-Ru}^{III}\text{-OH}^{2+} + OAc^- \leftrightarrow \{\text{nanoITO-Ru}^{III}\text{-OH}^{2+}\cdots OAc^-\}^+. \quad \textbf{[4a]}$$

$$\{\text{nanoITO-Ru}^{III}\text{-OH}^{2+}\cdots OAc^-\}^+ - e^- \rightarrow \{\text{nanoITO-Ru}^{IV}{=}O^{2+}\cdots HOAc\}^{2+}. \quad \textbf{[4b]}$$

$$\{\text{nanoITO-Ru}^{IV}{=}O^{2+}\cdots HOAc\}^{2+} \leftrightarrow \text{nanoITO-Ru}^{IV}{=}O^{2+} + HOAc. \quad \textbf{[4c]}$$

The importance of preliminary ion pairing is shown by the influence of added KNO_3 (Fig. 3*B*). In these experiments, CVs of nanoITO|**2-PO$_3$H$_2$** ($\Gamma/\Gamma_o = 0.40$) at pH 5 (0.1 M $HOAc/OAc^-$) with increasing amounts of added KNO_3 were obtained at 10 mV/s. Under these conditions, the ratio of peak currents for the two oxidative waves, $i_{p,a}(1.0\text{ V})/i_{p,a}(1.26\text{ V})$, decreases as $[NO_3^-]$ is increased from 0 to 1 M. The implied conversion in surface mechanism from EPT with OAc^- as acceptor base to

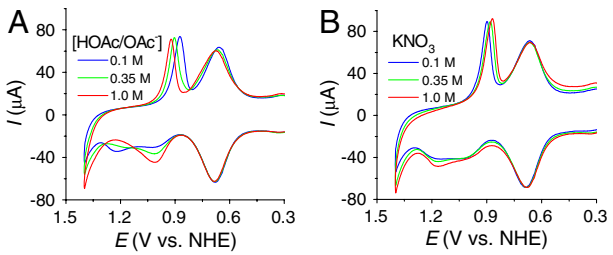

Fig. 3. (*A*) CVs of nanoITO|**2-PO$_3$H$_2$** ($\Gamma/\Gamma_o = 0.35$) at pH 5 with different concentrations of HOAc/NaOAc. (*B*) CVs of nanoITO|**2-PO$_3$H$_2$** ($\Gamma/\Gamma_o = 0.40$) at pH 5 (0.1 M $HOAc/OAc^-$) with addition of increasing amounts of KNO_3. Scan rate, 10 mV/s; temperature, 22 °C.

direct oxidation is consistent with a generalized ion atmosphere effect and/or replacement of OAc^- by NO_3^- at the ion paired surface cation (7). $E_{p,c}$ for Ru(IV → III) rereduction also shifts negatively with increasing NO_3^- because of competitive ion pairing with NO_3^-.

H_2O/D_2O Kinetic Isotope Effects. At pH 5, notable H_2O/D_2O isotope effects appear for the Ru(III → IV) wave on nanoITO|**2-PO_3H_2** ($\Gamma/\Gamma_o = 1$), whereas the Ru(II → III) wave is essentially unaffected (Fig. 4). In D_2O, $i_{p,a}$ for Ru^{III}-OH^{2+} → Ru^{IV}=O^{2+} oxidation at $E_{p,a} = 1.0$ V is greatly decreased, whereas $i_{p,a}$ for direct Ru^{III}-OH^{2+} → $Ru^{IV}(OH)^{3+}$ oxidation at $E_{p,a} = 1.26$ V is increased.

The isotopic discrimination between pathways is a reflection of surface mechanism. As shown by measurements at pH 1 in *SI Appendix*, Fig. S8, there is essentially no KIE for direct Ru^{III}-OH^{2+} → $Ru^{IV}(OH)^{3+}$ oxidation with $i_{p,a}(H_2O)/i_{p,a}(D_2O) = \sim 1$ independent of surface coverage. By contrast, at pH 5 for the wave at $E_{p,a} = 1.0$ V in Fig. 4*A*, $i_{p,a}(H_2O)/i_{p,a}(D_2O) = \sim 2.4$ comparable to the KIE observed for oxidation of *cis*-$[Os^{III}(bpy)_2(py)(OH)]^{2+}$ with added buffer bases (7).

At pH 5, there are two mechanistic contributors to the wave for Ru^{III}-OH^{2+} → Ru^{IV}=O^{2+} oxidation at $E_{p,a} = 1.0$ V. Cross-surface disproportionation, [**3**], is dominant with an additional contribution from the EPT pathway in [**4**]. Participation by two pathways appears in the nonlinearity of the plot of $i_{p,a}$ vs. mole fraction of D_2O (X_{D_2O}) (Fig. 4*B*). A linear relationship is predicted for a single pathway with a single proton transferred (2). At a lower surface coverage, $\Gamma/\Gamma_o = 0.60$, where EPT should play a greater role, KIE = ~3.6.

As noted above, at pH 1, electron transfer dominates with KIE = ~1. There is a slight but noticeable shift in $E_{1/2}$ for this wave from 1.27 V at $X_{D_2O} = 0$ to 1.33 V at $X_{D_2O} = 1$ (*SI Appendix*, Fig. S8). Given the proton content change for the Ru^{III}-OH_2^{2+}/$Ru^{IV}(OH)^{3+}$ couple at this pH, the shift in $E_{1/2}$, $\Delta E_{1/2}$ is dominated by the proton equilibrium in [**2a**]. In this limit, $\Delta E_{1/2} = 0.06\ V = 0.059\{pK_a(Ru^{III}\text{-}OH_2^{3+}) - pK_a(Ru^{III}\text{-}OD_2^{3+})\}$. With $pK_a(Ru^{III}\text{-}OH_2^{3+}) = 2.5$ (*SI Appendix*, Fig. S1), $pK_a(Ru^{III}\text{-}OD_2^{3+})$ is estimated to be 1.3.

Rereduction of Ru^{IV}=O^{2+}. For nanoITO|**2-PO_3H_2** or FTO|**2-PO_3H_2** in acidic solution, a kinetically inhibited, but normal wave shape is observed for $Ru^{IV}(OH)^{3+}$ → Ru^{III}-OH_2^{3+} rereduction at $E_{1/2} = 1.27$ V. Under these conditions, the mechanism for rereduction is ET-PT, the reverse of [**2**].

At higher pHs, with pH > $pK_a(Ru^{IV}(OH)^{3+})$, the equilibrium concentration of $Ru^{IV}(OH)^{3+}$ is reduced and rereduction by ET-PT, the reverse of [**2**], becomes insignificant. Under these conditions, Ru(IV → III) rereduction occurs by a skewed, narrow wave at lower potentials. Its $E_{p,c}$ value is dependent on surface loading, scan rate, and base concentration.

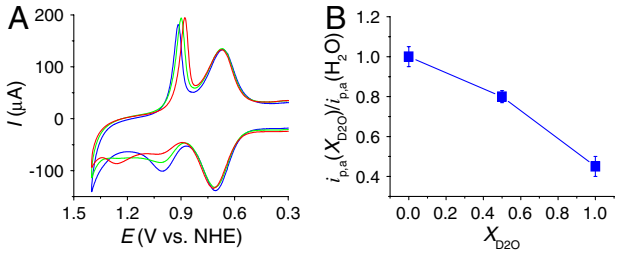

Fig. 4. (*A*) CVs of nanoITO|**2-PO_3H_2** ($\Gamma/\Gamma_o = 1$) at pH 5 (0.1 M $HOAc/OAc^-$) in H_2O (blue), 1:1 H_2O/D_2O (green), and D_2O (red). (*B*) Dependence of $i_{p,a}(X_{D_2O})/i_{p,a}(H_2O, X_{D_2O} = 0)$ at 1.0 V (background subtracted) on X_{D_2O}. Scan rate, 10 mV/s; temperature, 22 °C.

Rereduction of Ru^{IV}=O^{2+} is constrained to occur by ET-PT with reduction to Ru^{III}-O^+ followed by rapid protonation of Ru^{III}-O^+, [**5a**] and [**5b**]. The thermodynamic potential for the Ru^{IV}=O^{2+}/Ru^{III}-O^+ couple can be estimated from Eq. **6** and the difference in pK_a values between $Ru^{IV}(OH)^{3+}$ and Ru^{III}-OH^{2+}. Given that, $E^{o\prime}(Ru^{IV}(OH)^{3+}/Ru^{III}\text{-}OH^{2+}) = 1.27$ V, and assuming $pK_a(Ru^{IV}(OH)^{3+}) \approx 3$ and $pK_a(Ru^{III}\text{-}OH^{2+}) > 14$, $E^{o\prime}(Ru^{IV}{=}O^{2+}/Ru^{III}\text{-}O^+)$ is estimated to be <0.62 V. Based on this estimate for $E^{o\prime}(Ru^{IV}{=}O^{2+}/Ru^{III}\text{-}O^+)$ and the data in Fig. 2*A*, reduction at $E_{p,c} = \sim 0.83$ V at $\Gamma/\Gamma_o = 0.1$ (green line) at 10 mV/s occurs with an underpotential of >0.21 V.

$$\text{nanoITO-}Ru^{IV}{=}O^{2+} + e^- \rightarrow \text{nanoITO-}Ru^{III}\text{-}O^+. \qquad \textbf{[5a]}$$

$$\text{nanoITO-}Ru^{III}\text{-}O^+ + H^+ \rightarrow \text{nanoITO-}Ru^{III}\text{-}OH^{2+}(\text{rapid}). \qquad \textbf{[5b]}$$

$$\text{nanoITO-}Ru^{III}\text{-}OH^{2+} + e^- + H^+ \rightarrow \text{nanoITO-}Ru^{II}\text{-}OH_2^{2+}. \qquad \textbf{[5c]}$$

$$\text{nanoITO-}Ru^{IV}{=}O^{2+} + \text{nanoITO-}Ru^{II}\text{-}OH_2^{2+} \rightarrow 2\text{nanoITO-}Ru^{III}\text{-}OH^{2+}. \qquad \textbf{[5d]}$$

$$E^{o\prime}(Ru^{IV}{=}O^{2+}/Ru^{III}\text{-}O^+) = E^{o\prime}(Ru^{IV}(OH)^{3+}/Ru^{III}\text{-}OH^{2+}) + 0.059\{pK_a(Ru^{IV}(OH)^{3+}) - pK_a(Ru^{III}\text{-}OH^{2+})\}. \qquad \textbf{[6]}$$

From the surface loading dependence in Fig. 2*A*, there also appears to be an autocatalytic effect triggered by partial reduction arising from cross-surface comproportionation, [**5c**] and [**5d**]. With Ru^{III}-OH^{2+} formed by ET-PT reduction of Ru^{IV}=O^{2+}, [**5a**] and [**5b**], a basis for autocatalysis exists by further reduction to Ru^{II}-OH_2^{2+} and cross-surface comproportionation with the remaining Ru^{IV}=O^{2+} sites on the surface, [**5c**] and [**5d**]. As shown by the CV simulations in *SI Appendix*, Fig. S9 and Table S1, an analogous mechanism for the solution Ru^{IV}=O^{2+}/Ru^{III}-OH^{2+}/Ru^{II}-OH_2^{2+} couples of **2** at pH 5 reproduces the narrow wave shape observed for the surface couple.

Propylene Carbonate as Solvent. In propylene carbonate (PC) with added water (PC:H_2O, water miscibility <8%, vol:vol), both **2** and its surface analog, nanoITO|**2-PO_3H_2**, are known water oxidation catalysts by the mechanism in Scheme 2 (31). There is evidence for continued coordination of H_2O based on the UV-visible spectra of **2** in solution (31) and for **2-PO_3H_2** on nanoITO (see below).

There is also evidence for surface PCET effects based on the surface-bound phosphonate groups with $pK_a \sim 1$–2 for proton loss in water (12, 32). The procedure for surface attachment of **2-PO_3H_2**, described in *Materials and Methods* ("as prepared"), involved soaking the complex for extended periods at pH 5 (0.1 M $HOAc/OAc^-$) followed by rinsing with distilled water, conditions under which deprotonation of the phosphonates occurs to give nanoITO-$[\{(\text{-O})(O)_2PCH_2\}_2bpy)Ru^{II}(Mebimpy)(OH_2)]^0$ on the surface, [**7**] (12, 32). In aqueous solutions, proton equilibration between the surface-bound phosphonate groups and the external solution occurs rapidly. In dry PC, the surface proton composition is fixed and, as shown below, impacts CVs for both Ru(IV/III) and Ru(III/II) couples:

$$\text{nanoITO-}[\{(\text{-O})(O)(OH)PCH_2\}_2bpy)Ru^{II}(Mebimpy)(OH_2)]^{2+} \leftrightarrow \text{nanoITO-}[\{(\text{-O})(O)_2PCH_2\}_2bpy)Ru^{II}(Mebimpy)(OH_2)]^0 + 2H^+. \qquad \textbf{[7]}$$

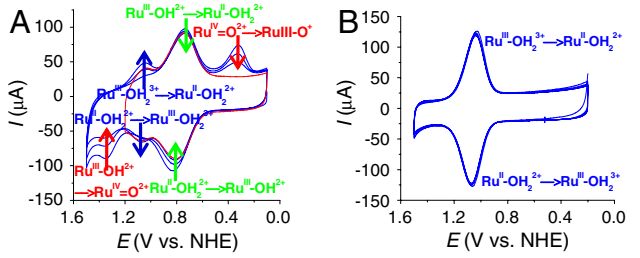

Fig. 5. (*A*) Successive CVs (three cycles) of as-prepared nanoITO|**2-PO$_3$H$_2$** ($\Gamma/\Gamma_o = 1$) in 0.1 M $LiClO_4$/PC. The arrows indicate the current variations upon successive potential scans. Red line, potential scan reversal before $E_{p,a} = 1.33$ V. (*B*) Successive CVs (five cycles) of acid-treated nanoITO|**2-PO$_3$H$_2$** ($\Gamma/\Gamma_o = 1$) in 0.1 M $LiClO_4$/PC. Scan rate, 10 mV/s; temperature, 22 °C.

A CV for an as-prepared nanoITO|**2-PO$_3$H$_2$** slide is shown in Fig. 5*A* in 0.1 M $LiClO_4$/PC at 10 mV/s. In the first scan, a wave for a Ru(III/II) couple appears, but at $E_{1/2} = 0.78$ V ($\Delta E_p = 90$ mV) with a relatively small, irreversible Ru(III → IV) wave at $E_{p,a} = 1.33$ V. The potential difference between Ru (II → III) and Ru(III → IV) waves is $\Delta E_{p,a} \sim 500$ mV, which is comparable to $\Delta E_{p,a} \sim 400$ mV between Ru^{II}-OH_2^{2+} → Ru^{III}-OH^{2+} and Ru^{III}-OH^{2+} → Ru^{IV}=O^{2+} oxidations at pH 5, suggesting a common origin.

Following successive scans through the Ru^{III}-OH^{2+} → Ru^{IV}=O^{2+} wave accompanied by proton release, a new Ru(III/II) couple appears at $E_{1/2} = 1.06$ V ($\Delta E_p = 40$ mV). This wave arises from the Ru^{III}-OH_2^{3+}/Ru^{II}-OH_2^{2+} couple (see below), with its $E_{1/2}$ value increased by 240 mV compared to $E_{1/2} = 0.82$ V for the same couple in 0.1 M HNO_3 (Fig. 2*B*). Appearance of the Ru^{III}-OH_2^{3+}/Ru^{II}-OH_2^{2+} couple is accompanied by decreases in peak currents for the Ru^{III}-OH^{2+}/Ru^{II}-OH_2^{2+} couple at $E_{1/2} = 0.78$ V and the Ru^{III}-OH^{2+} → Ru^{IV}=O^{2+} wave at $E_{p,a} = 1.33$ V.

A CV for an "acid treated" nanoITO|**2-PO$_3$H$_2$** slide is shown in Fig. 5*B*. In the acid treatment, an as-prepared slide was soaked in a 0.1 M $HClO_4$ aqueous solution for 30 s followed by drying in a N_2 gas stream. In the resulting CV in 0.1 M $LiClO_4$/PC at 10 mV/s, a wave for the Ru^{III}-OH_2^{3+}/Ru^{II}-OH_2^{2+} couple appears at $E_{1/2} = 1.06$ V ($\Delta E_p = 40$ mV) with no evidence for further oxidation to Ru^{IV}=O^{2+} through a series of five successive scans. Surface oxidation of Ru^{II}-OH_2^{2+} to Ru^{III}-OH_2^{3+} rather than Ru^{III}-OH^{2+} is the expected result in a nonaqueous solvent with a significant decrease in proton acidity for Ru^{III}-OH_2^{3+} due to loss of hydration free energy for the proton (33).

An explanation is available for the difference in behaviors between as-prepared and acid-treated slides and the appearance of the proton-dependent Ru^{II}-OH_2^{2+}/Ru^{III}-OH^{2+} and Ru^{III}-OH^{2+} → Ru^{IV}=O^{2+} waves based on PCET involvement by basic sites on the surface or, more likely, the surface-bound, phosphonate groups with $pK_a \sim 1$–2. The deprotonated phosphonate groups on as-prepared slides presumably act as proton acceptors for Ru^{II}-OH_2^{2+} → Ru^{III}-OH^{2+} oxidation with proton transfer to a surface phosphonate group (step 1 in Scheme 3). The Ru^{III}-OH^{2+}/Ru^{II}-OH_2^{2+} couple is kinetically inhibited, presumably because of the requirements imposed on proton transfer by orientation and proton transfer distance. Kinetic inhibition is seen in the increase in ΔE_p from 40 mV for the same couple at pH 5 (0.1 M HOAc/OAc^-) in water compared to 90 mV in PC and by the scan rate dependence of the couple (*SI Appendix*, Fig. S10). At fast scan rates, Ru^{II}-$OH_2^{2+} - e^- - H^+$ → Ru^{III}-OH^{2+} oxidation is incomplete at the thermodynamic potential for the couple. Sites that remain unoxidized at $E_{p,a} = 0.83$ V undergo Ru^{II}-$OH_2^{2+} - e^-$ → Ru^{III}-OH_2^{3+} oxidation at $E_{p,a} = 1.08$ V.

Given the proton stoichiometry in [**7**], an additional deprotonated phosphonate site is available at as-prepared slides for further oxidation and proton loss, enabling access to Ru^{IV}=O^{2+} (step 2 in Scheme 3), which would explain the appearance of the wave at $E_{p,a} = 1.33$ V as due to Ru^{III}-OH^{2+} → Ru^{IV}=O^{2+} oxidation. Oxidation occurs only through Ru^{III}-OH^{2+} and not through Ru^{III}-OH_2^{3+} as shown by the absence of a Ru(III → IV) wave for the acid-treated slide in Fig. 5*B*. Surface-bound phosphonates may also play a role in the aqueous solution electrochemistry of the surface-bound Ru(IV/III) couple but with no evidence for it in our data.

The Ru^{II}-OH_2^{2+} → Ru^{III}-OH_2^{3+} wave appears for as-prepared slides only on successive oxidative scans (Fig. 5*A*). It appears to be triggered by Ru^{III}-OH^{2+} → Ru^{IV}=O^{2+} oxidation and proton release. Presumably, partial protonation of surface phosphonate sites inhibits Ru^{II}-OH_2^{2+} → Ru^{III}-OH^{2+} oxidation with unoxidized sites undergoing Ru^{II}-OH_2^{2+} → Ru^{III}-OH_2^{3+} oxidation at $E_{p,a} = 1.08$ V.

The phenomena reported in Fig. 5 are independent of surface loading with closely related observations made at $\Gamma/\Gamma_o = 0.2$ (*SI Appendix*, Fig. S11). There is no evidence for cross-surface disproportionation in PC as solvent, presumably because the PCET-phosphonate pathways in Scheme 3 are kinetically more facile and dominate electron transfer reactivity of the surface Ru(IV/III) couple.

As shown by the switching potential variations in Fig. 5*A*, in PC, in the absence of a ready supply of protons, rereduction of Ru^{IV}=O^{2+} to Ru^{III}-O^+ occurs at $E_{p,c} = 0.34$ V at 10 mV/s. This value is consistent with $E^{o\prime} < 0.62$ V estimated for the Ru^{IV}=O^{2+}/Ru^{III}-O^+ couple in water by use of Eq. **6**. As shown in *SI Appendix*, Fig. S12 and Table S2, CV simulations of **2** in PC based on a mechanism involving Ru^{IV}=O^{2+} → Ru^{III}-O^+ reduction reproduces the Ru^{IV}=O^{2+} → Ru^{III}-O^+ waveform.

Both potential and peak current for Ru^{IV}=O^{2+} → Ru^{III}-O^+ rereduction are scan-rate dependent (*SI Appendix*, Fig. S10). As the scan rate is decreased, $E_{p,c}$ shifts positively and the current ratio $i_{p,c}(0.34\text{ V})/i_{p,a}(1.33\text{ V})$ decreases. These observations are qualitatively consistent with protonation of Ru^{III}-O^+ by trace water or protonated surface phosphonate following reduction of $Ru^{IV} = O^{2+}$ at slow scan rates.

The influence of added water on CVs of nanoITO|**2-PO$_3$H$_2$** ($\Gamma/\Gamma_o = 1$) in 0.1 M $LiClO_4$/PC is illustrated in Fig. 6. Increasing

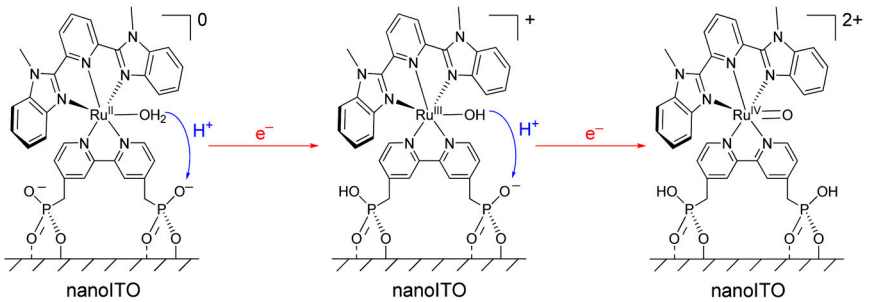

Scheme 3. Proposed interfacial proton transfer to surface phosphonate groups in the oxidation of Ru^{II}-OH_2^{2+} to Ru^{IV}=O^{2+} in PC as solvent.

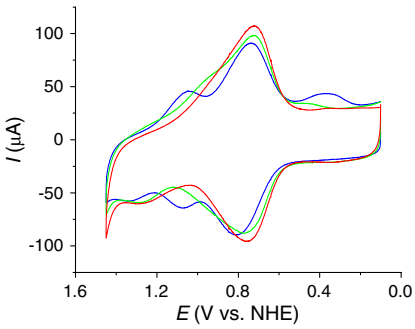

Fig. 6. CVs of nanoITO|**2-PO$_3$H$_2$** ($\Gamma/\Gamma_o = 1$) in 0.1 M $LiClO_4$/PC with addition of 0% (blue), 1% (green), and 6% (red) water. Scan rate, 10 mV/s; temperature, 22 °C.

water from 0% to 6% (vol:vol) causes a decrease in $E_{1/2}$ for the Ru^{III}-OH^{2+}/Ru^{II}-OH_2^{2+} couple from 0.78 to 0.73 V, presumably due to a generalized solvation effect. The peak currents for the Ru^{III}-OH^{2+}/Ru^{II}-OH_2^{2+} couple also grow at the expense of i_p for the Ru^{III}-OH_2^{3+}/Ru^{II}-OH_2^{2+} couple, presumably due to the PCET couple being favored by enhanced solvation of the released proton.

Solvation also affects Ru^{III}-$OH^{2+} \rightarrow Ru^{IV}{=}O^{2+}$ oxidation with $E_{p,a} = 1.33$ V (0% H_2O) shifting to 1.28 V (6% H_2O). The influence of water is more profound on the $Ru^{IV}{=}O^{2+} \rightarrow Ru^{III}$-$O^+$ reduction wave because of rapid protonation of Ru^{III}-O^+ once it is formed with $E_{p,c}$ shifting to 0.46 V with 1% added water. At 6% added water, this wave is shifted more positively and masked by the Ru^{III}-$OH^{2+} \rightarrow Ru^{II}$-$OH_2^{2+}$ reduction wave.

Comparisons with nanoITO|1-PO$_3$H$_2$. CV measurements were extended to the Ru(IV/III) couple of **1-PO$_3$H$_2$** on nanoITO. As noted in the Introduction, $\Delta E^{o\prime} = 0.09$ V between the Ru (IV/III) and Ru(III/II) couples for **1-PO$_3$H$_2$** from pH 1 to pH 10. The Ru^{III}-OH_2^{3+} form of **1-PO$_3$H$_2$** is more acidic than **2-PO$_3$H$_2$** with $pK_a(Ru^{III}\text{-}OH_2^{3+}) \sim 1.4$ (11).

In Fig. 7 are shown CVs of nanoITO|**1-PO$_3$H$_2$** at three different surface loadings in three different media. For the surfaces with $\Gamma/\Gamma_o \leq 0.4$ in 1 M $HClO_4$ (red and green lines in Fig. 7*A*), a chemically reversible but kinetically distorted wave appears for the Ru(IV/III) couple at $E_{1/2} = 1.28$ V. This wave appears at the expected $E_{1/2}$ value for the $Ru^{IV}(OH)^{3+}$/Ru^{III}-OH_2^{3+} couple for **1-PO$_3$H$_2$** at this pH. On these dilute surfaces, a reasonable mechanism for Ru^{III}-$OH_2^{3+} \rightarrow Ru^{IV}(OH)^{3+}$ oxidation is PT-ET, as proposed in [**2**] for **2-PO$_3$H$_2$**. $Ru^{IV}(OH)^{3+} \rightarrow Ru^{III}$-$OH_2^{2+}$ rereduction at 10 mV/s occurs at $E_{p,c} = 1.17$ V with a relatively normal wave shape, but the couple is kinetically inhibited with $\Delta E_p = 230$ mV.

On a completely loaded surface ($\Gamma/\Gamma_o = 1$) (blue line in Fig. 7*A*), there is evidence for dual pathways based on the appearance of a new wave at $E_{p,a} = \sim 1.30$ V at 10 mV/s. The surface loading dependence is consistent with the disproportionation mechanism in [**3**] and the appearance of dual pathways to a competition between disproportionation in [**3**] and direct oxidation in [**2**]. On the reverse scan, a narrow rereduction wave appears at $E_{p,a} = 1.23$ V (blue line in Fig. 7*A*). The wave shape is similar to that for rereduction of $Ru^{IV}{=}O^{2+}$ for **2-PO$_3$H$_2$** at pH 5 (0.1 M HOAc/OAc^-) and the autocatalytic mechanism in [**5**].

At pH 1 (0.1 M $HClO_4$) at 10 mV/s, there is clearer evidence for surface loading-dependent, dual pathways for Ru(III → IV) oxidation with waves appearing at $E_{p,a} = 1.36$ and 1.19 V (Fig. 7*B* and *SI Appendix*, Fig. S13). For the wave at $E_{p,a} = 1.19$, $i_{p,a}$ increases as surface coverage is increased, consistent with disproportionation in competition with direct oxidation. The disproportionation pathway dominates at $\Gamma/\Gamma_o = 1$. A single, narrow, surface loading-dependent rereduction wave appears with $E_{p,c} = 1.16$ V at $\Gamma/\Gamma_o = 1$, consistent with autocatalytic comproportionation, [**5**].

Related phenomena were observed at pH 5 (0.1 M HOAc/OAc^-) at 10 mV/s. A wave for direct Ru(III → IV) oxidation appears at $E_{p,a} = 1.33$ V ($\Gamma/\Gamma_o \leq 0.1$) (the CV in red in Fig. 7*C* with a magnified view in *SI Appendix*, Fig. S14). At higher surface coverages, disproportionation dominates with Ru^{III}-$OH^{2+} \rightarrow Ru^{IV}{=}O^{2+}$ oxidation occurring at $E_{p,a} = 0.98$ V. Reverse, Ru (IV → III) rereduction also occurs by a single, narrow, surface loading-dependent wave with $E_{p,c} = 0.90$ V at $\Gamma/\Gamma_o = 1$. As noted above, disproportionation is expected to play a more important role than at nanoITO|**2-PO$_3$H$_2$** because of the small driving force ($\Delta G = +0.09$ eV) for Ru^{III}-OH^{2+} disproportionation.

As shown in *SI Appendix*, Fig. S15, CVs of nanoITO|**2-PO$_3$H$_2$** in 0.1 M $LiClO_4$/PC have the same features as described for nanoITO|**1-PO$_3$H$_2$**, consistent with participation by the surface-bound phosphonate groups in PCET half reactions.

Real Time Spectrophotometric Study. The use of optically transparent, conductive, high surface area nanoITO allows for the acquisition of UV-visible spectral data of electrochemically generated intermediates and for direct spectral monitoring of voltammograms (34, 35). Fig. 8 shows spectra acquired for nanoITO|**2-PO$_3$H$_2$** ($\Gamma/\Gamma_o = 1$) at a series of potentials during CV scans (see Fig. 2). CV scans at fixed wavelengths are shown in *SI Appendix*, Fig. S16.

In 0.1 M HNO_3 (Fig. 8*A*), potential scans to 1.08 V, past $E_{1/2} = 0.82$ V for Ru(II → III) oxidation, results in loss of the $\lambda_{max} = 494$ nm metal-to-ligand charge transfer (MLCT) absorption, a characteristic feature for surface-bound Ru^{II}-OH_2^{2+}. A ligand-to-metal charge transfer (LMCT) absorption for Ru^{III}-OH_2^{3+} appears at $\lambda_{max} = \sim 650$ nm with an increase in absorbance at 400 nm. A further increase in potential to 1.4 V, past $E_{1/2} = 1.27$ V for Ru(III → IV) oxidation, results in a broad absorption at approximately 500 nm for $Ru^{IV}(OH)^{3+}$ and the appearance of a shoulder at approximately 400 nm, which appear concomitantly with the disappearance of the absorption of Ru^{III}-OH_2^{3+}. These spectral changes are consistent with those obtained for stepwise oxidation of $[Ru^{II}(Mebimpy)(bpy)(OH_2)]^{2+}$ to Ru^{III}-OH_2^{3+} and then to $Ru^{IV}(OH)^{3+}$ by incremental addition of Ce(IV) in 0.1 M HNO_3 (20, 21). The spectra and spectral changes are reversible through multiple scans (*SI Appendix*, Fig. S16*A*).

In 0.1 M HOAc/OAc^- at pH 5 (Fig. 8*B*), scans past $E_{1/2} = 0.68$ V for the Ru(III/II) couple result in loss of the Ru^{II}-

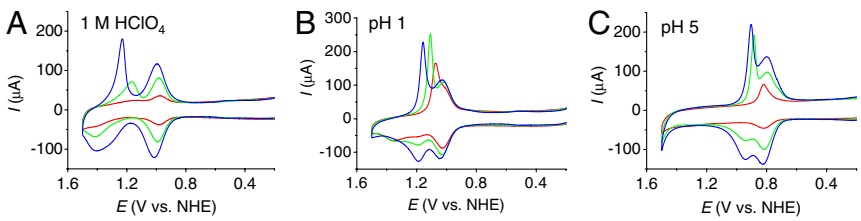

Fig. 7. CVs of nanoITO|**1-PO$_3$H$_2$** with (*A*) $\Gamma/\Gamma_o = 0.1$ (red), 0.4 (green), 1 (blue) in 1 M $HClO_4$, (*B*) $\Gamma/\Gamma_o = 0.25$ (red), 0.6 (green), 1 (blue) at pH 1 (0.1 M $HClO_4$), and (*C*) $\Gamma/\Gamma_o = 0.1$ (red), 0.6 (green), 1 (blue) at pH 5 (0.1 M HOAc/OAc^-). Scan rate, 10 mV/s; temperature, 22 °C.

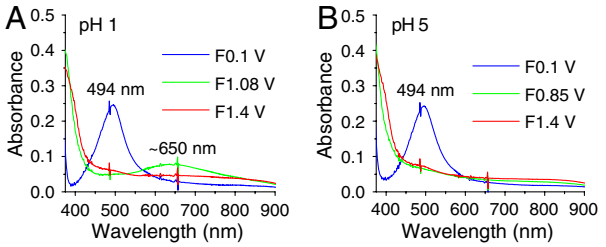

Fig. 8. UV-visible spectra of nanoITO|**1-PO_3H_2** ($\Gamma/\Gamma_o = 1$) scanned to different potentials as indicated (F, forward scan; see Fig. 2). Solution, (*A*) pH 1 (0.1 M HNO_3), (*B*) pH 5 (0.1 M HOAc/OAc^-). Scan rate, 10 mV/s; temperature, 22 °C.

OH_2^{2+} absorption at $\lambda_{max} = 494$ nm, consistent with oxidation to Ru^{III}-OH^{2+}. The latter is relatively featureless in the visible but increases in absorbance at approximately 400 nm. A further increase in potential to 1.4 V, past $E_{1/2}$ for the Ru(IV/III) couple, results in growth of the approximately 500 nm absorbance and approximately 400 nm shoulder for $Ru^{IV}=O^{2+}$. Reversal of the potential scan from 1.4 to 0.1 V results in complete recovery of the original spectrum (*SI Appendix*, Fig. S16*B*).

Fig. 9 shows spectra at nanoITO|**2-PO_3H_2** ($\Gamma/\Gamma_o = 1$) obtained at fixed potentials during CV scans (see Fig. 5) in 0.1 M $LiClO_4$/PC. CV scans monitored at fixed wavelengths are shown in *SI Appendix*, Fig. S17. The spectral profiles obtained for Ru^{II}-OH_2^{2+} and Ru^{III}-OH_2^{3+} in PC are consistent with profiles in water but with λ_{max} blue shifted by approximately 2 nm because of a generalized solvent effect.

At the acid-treated slide in Fig. 9*A*, with surface potential scanned to 1.3 V, past $E_{1/2} = 1.06$ V for the Ru(III/II) couple in PC, the MLCT absorption for Ru^{II}-OH_2^{2+} at $\lambda_{max} = 492$ nm decreases with an increase in LMCT absorption for Ru^{III}-OH_2^{3+} at $\lambda_{max} = \sim 648$ nm, consistent with oxidation from Ru^{II}-OH_2^{2+} to Ru^{III}-OH_2^{3+}. There were no further spectral changes upon increasing the potential to 1.5 V, consistent with the inaccessibility of $Ru^{IV}=O^{2+}$ on the acid-treated slide. Reversal of the potential scan from 1.5 to 0.1 V results in complete recovery of the original spectrum (*SI Appendix*, Fig. S17*A*).

The spectral evolution of an as-prepared slide in PC as solvent is complicated by participation by both the Ru^{III}-OH^{2+}/Ru^{II}-OH_2^{2+} and Ru^{III}-OH_2^{3+}/Ru^{II}-OH_2^{2+} couples and by Ru^{III}-$OH^{2+} \rightarrow Ru^{IV}=O^{2+}$ oxidation (Fig. 9*B*). With the surface potential scanned to 1.0 V, past $E_{1/2} = \sim 0.78$ V for the Ru^{III}-OH^{2+}/Ru^{II}-OH_2^{2+} couple, the MLCT absorption at $\lambda_{max} = 492$ nm decreases partially with no evidence for Ru^{III}-OH_2^{3+} at $\lambda_{max} = \sim 648$ nm, consistent with oxidation to Ru^{III}-OH^{2+}. Increasing the potential to 1.2 V, past $E_{1/2} = \sim 1.06$ V for the Ru^{III}-OH_2^{3+}/Ru^{II}-OH_2^{2+} couple, results in further loss of the MLCT absorption band at $\lambda_{max} = 492$ nm concomitant with appearance of the LMCT band at $\lambda_{max} = \sim 648$ nm for Ru^{III}-OH_2^{3+}, consistent with oxidation of the remaining Ru^{II}-OH_2^{2+} sites to Ru^{III}-OH_2^{3+}. A further increase in potential to 1.5 V, past

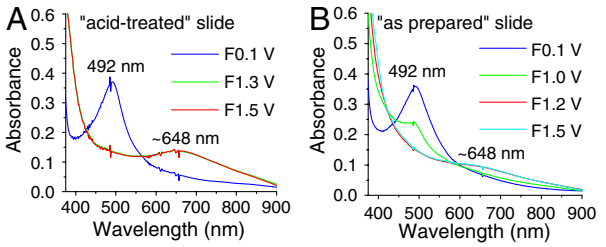

Fig. 9. UV-visible spectra of (*A*) acid-treated and (*B*) as-prepared nanoITO|**2-PO_3H_2** ($\Gamma/\Gamma_o = 1$) in 0.1 M $LiClO_4$/PC scanned to different potentials as indicated (F, forward scan; see Fig. 5). Scan rate, 10 mV/s; temperature, 22 °C.

$E_{p,a} = \sim 1.33$ V for Ru^{III}-$OH^{2+} \rightarrow Ru^{IV}=O^{2+}$ oxidation results in a slight growth at $\lambda = \sim 400$–500 nm for $Ru^{IV}=O^{2+}$ as observed in aqueous solution. In the additional oxidation to $Ru^{IV}=O^{2+}$, the LMCT absorption at $\lambda_{max} = 648$ nm for Ru^{III}-OH_2^{3+} is nearly unaffected, consistent with oxidation from Ru^{III}-OH^{2+} to $Ru^{IV}=O^{2+}$, but not from Ru^{III}-OH_2^{3+}. This result is consistent with the CV result described in the previous section. The fixed wavelength spectral evolution shown in *SI Appendix*, Fig. S17*B* reveals a series of spectral changes for the MLCT absorption band at $\lambda_{max} = 492$ nm, consistent with the sequence of electrochemical/chemical events suggested in the figure.

Conclusions

The overall water oxidation cycle in Scheme 2 consists of a linear sequence of reactions. In order to maximize rates, it is essential that activation barriers for the key rate limiting step or steps be minimized. For water oxidation in Scheme 2, a potential kinetic bottleneck appears in the oxidative activation sequence from Ru^{II}-OH_2^{2+} to $Ru^{V}=O^{3+}$ in the Ru^{III}-OH_2^{3+}, Ru^{III}-$OH^{2+} \rightarrow Ru^{IV}(OH)^{3+}$, $Ru^{IV}=O^{2+}$ stage. Its origin is PCET and the significant change in pK_a that exists between Ru^{III}-OH^{2+} and $Ru^{IV}(OH)^{3+}$. In an overall catalytic scheme, slow rates for this step could compete with the O···O bond-forming step between $Ru^{V}=O^{3+}$ and H_2O and limit catalytic rates and efficiencies. The results presented here highlight the origin of kinetic inhibitions and provide insights into how to overcome them.

1. Oxidative activation of Ru^{III}-OH^{2+} (in proton equilibrium with Ru^{III}-OH_2^{3+}) to $Ru^{IV}(OH)^{3+}$ can occur by PT-ET. A pH-dependent overpotential exists for this pathway. It arises from the difference in $E_{1/2}$ values between the $Ru^{IV}(OH)^{3+}$/Ru^{III}-OH^{2+} and $Ru^{IV}=O^{2+}$/Ru^{III}-OH^{2+} couples.
2. On highly loaded surfaces, cross-surface disproportionation of Ru^{III}-OH^{2+} occurs to give $Ru^{IV}=O^{2+}$. Disproportionation is followed by oxidation of Ru^{II}-OH_2^{2+} on the surface and proton equilibration by Ru^{III}-OH_2^{3+}. The kinetic facility of this pathway is dictated, in part, by the difference in $E_{1/2}$ values between the $Ru^{IV}=O^{2+}$/Ru^{III}-OH^{2+} and Ru^{III}-OH^{2+}/Ru^{II}-OH_2^{2+} couples.
3. Concerted EPT with added acid-base buffer pairs like HOAc/OAc^- can facilitate Ru^{III}-$OH^{2+} \leftrightarrow Ru^{IV}=O^{2+}$ interconversion by avoiding Ru^{III}-O^+ and $Ru^{IV}(OH)^{3+}$ as high-energy intermediates.
4. As shown by both CV and spectroelectrochemical results, in propylene carbonate, access to $Ru^{IV}=O^{2+}$ depends on the initial protonation state of the phosphonate groups at the electrode surface. With these sites protonated, oxidation stops at Ru^{III}-OH_2^{3+} and there is no access to $Ru^{IV}=O^{2+}$. With deprotonated phosphonates at the surface, partial oxidation of Ru^{II}-OH_2^{2+} to Ru^{III}-OH^{2+} occurs with proton transfer to a phosphonate. Oxidation to Ru^{III}-OH^{2+} is followed by further oxidation to $Ru^{IV}=O^{2+}$ and proton transfer to a phosphonate. For a second fraction of surface Ru^{II}-OH_2^{2+} sites, proton transfer is inhibited on the CV timescale and oxidation gives Ru^{III}-OH_2^{3+} with no further oxidation to $Ru^{IV}=O^{2+}$.

$Ru^{IV}=O^{2+}$ rereduction presents related mechanistic challenges:

1. Reduction of $Ru^{IV}(OH)^{3+}$ to Ru^{III}-OH_2^{3+} can occur by ET-PT with $Ru^{IV}(OH)^{3+}$ reduction to Ru^{III}-OH^{2+} followed by proton equilibration to Ru^{III}-OH_2^{3+}. In water, this pathway only appears in relatively strongly acidic solutions where there is a kinetically significant concentration of $Ru^{IV}(OH)^{3+}$.
2. Underpotential reduction of $Ru^{IV}=O^{2+}$ occurs without initial protonation by narrow, kinetically skewed waves. At high surface coverages, autocatalytic reduction of $Ru^{IV}=O^{2+}$

occurs by partial reduction to Ru^{III}-O^{+} followed by rapid protonation, further reduction to Ru^{II}-OH_2^{2+}, and cross-surface comproportionation.

3. In PC with no added water, direct $Ru^{IV}{=}O^{2+} \rightarrow Ru^{III}$-$O^{+}$ reduction occurs at $E_{p,c} = 0.34$ V at 10 mV/s by a wave that shifts to positive potentials with added water.

Materials and Methods

Materials. Nitric acid (70%, redistilled, trace metal grade), acetic acid (99.9%), sodium acetate (> = 99%), deuterium oxide (D_2O, 99.9%), $RuCl_3{\bullet}3H_2O$, and 2,2′-bipyridine (>99%) were purchased from Sigma-Aldrich and used as received. Syntheses of salts of complex **2** and its phosphonated analog **2-PO_3H_2** were reported elsewhere (36). Complex **1** and its phosphonated analog **1-PO_3H_2** were prepared by similar methods but with $[Ru(tpy)]Cl_3$ as the precursor. All solutions were prepared with Milli-Q ultrapure water (>18 MΩ).

FTO glass (*Rs* = 7–8 Ω) was obtained from Hartford Glass Company, Inc., and ITO glass (*Rs* = 4–8 Ω) was purchased from Delta Technologies. NanoITO powder (40-nm diameter) was obtained from Lihochem. Optically transparent, electrically conductive, high surface area nanoITO films were prepared as described previously (34, 35). The resulting films are light blue and approximately 2.5 μm in thickness with a resistance of *Rs* = ∼200 Ω across 1 cm of the film by a two-point probe measurement on a borosilicate glass substrate. TiO_2 colloids (10- to 20-nm diameter) and semiconductive TiO_2-coated FTO slides (10 μm in film thickness) were prepared according to literature procedures (37).

Instrumentation. UV-visible spectra were recorded on an Agilent Technologies Model 8453 diode-array spectrophotometer. Electrochemical measurements were performed with the model CHI660D electrochemical workstation (CH Instruments). The three-electrode system consisted of a glass slide (area 1.25 cm^2) working electrode, a Pt mesh counter electrode, and an SCE reference electrode (approximately 0.244 V vs. NHE at 22 °C and approximately 0.20 V vs. NHE at 80 °C). (Temperature coefficient $(\partial E/\partial T) = -0.76$ mV/K was applied for correction.)

Procedures. Stable phosphonate surface binding of **2-PO_3H_2** on planar FTO to give FTO|**2-PO_3H_2**, on nanoITO films to give nanoITO|**2-PO_3H_2** or on nanoTiO_2 films to give nanoTiO_2|**2-PO_3H_2** occurred following immersion of the slides in solutions 0.2 mM in phosphonated complex at pH 5 (0.1 M $CH_3CO_2H/CH_3CO_2^-$, HOAc/OAc^-). The slides were thoroughly rinsed with distilled water to remove physically adsorbed complex, followed by drying under a N_2 gas stream. The extent of surface loading was varied by varying the soaking time with complete coverage after 2 h for FTO and 4 h for nanoITO and nanoTiO_2. Table 1 lists saturated surface coverages, Γ_o in mole per square centimeter, for **2-PO_3H_2** derivatized FTO, nanoITO, and nanoTiO_2. Surface binding by **1-PO_3H_2** utilized the same procedure.

ACKNOWLEDGMENTS. Funding by Army Research Office through Grant W911NF-09-1-0426 (to Z.C.), the University of North Carolina Energy Frontier Research Center (EFRC) Solar Fuels and Next Generation Photovoltaics, an EFRC funded by the US Department of Energy, Office of Science, Office of Basic Energy Sciences, under Award DE-SC0001011 (to J.J.C. and J.W.J.), and the Center for Catalytic Hydrocarbon Functionalization, an EFRC funded by the US Department of Energy under Award DE-SC0001298 at the University of Virginia (to A.K.V.) is gratefully acknowledged.

1. Costentin C, Robert M, Savéant JM (2010) Concerted proton-electron transfers: Electrochemical and related approaches. *Acc Chem Res* 43:1019–1029.
2. Huynh MHV, Meyer TJ (2007) Proton-coupled electron transfer. *Chem Rev* 107:5004–5064.
3. Hammes-Schiffer S (2009) Theory of proton-coupled electron transfer in energy conversion processes. *Acc Chem Res* 42:1881–1889.
4. Warren JJ, Tronic TA, Mayer JM (2010) Thermochemistry of proton-coupled electron transfer reagents and its implications. *Chem Rev* 110:6961–7001.
5. Petek H, Zhao J (2010) Ultrafast interfacial proton-coupled electron transfer. *Chem Rev* 110:7082–7099.
6. Binstead RA, Meyer TJ (1987) Hydrogen-atom transfer between metal complex ions in solution. *J Am Chem Soc* 109:3287–3297.
7. Costentin C, Robert M, Savéant JM, Teillout AL (2009) Concerted proton-coupled electron transfers in aquo/hydroxo/oxo metal complexes: Electrochemistry of $[Os^{II}(bpy)_2py(OH_2)]^{2+}$ in water. *Proc Natl Acad Sci USA* 106:11829–11836.
8. Thorp HH, Sarneski JE, Brudvig GW, Crabtree RH (1989) Proton-coupled electron transfer in manganese complex $[(bpy)_2Mn(O)_2Mn(bpy)_2]^{3+}$. *J Am Chem Soc* 111:9249–9250.
9. Lyon LA, Hupp JT (1999) Energetics of the nanocrystalline titanium dioxide aqueous solution interface: Approximate conduction band edge variations between $H_0 = -10$ and $H_- = +26$. *J Phys Chem B* 103:4623–4628.
10. Cabaniss GE, Diamantis AA, Murphy WR, Linton JRW, Meyer TJ (1985) Electrocatalysis of proton-coupled electron-transfer reactions at glassy carbon electrodes. *J Am Chem Soc* 107:1845–1853.
11. Trammell SA, et al. (1998) Mechanisms of surface electron transfer. Proton-coupled electron transfer. *J Am Chem Soc* 120:13248–13249.
12. Gagliardi CJ, Jurss JW, Thorp HH, Meyer TJ (2011) Surface activation of electrocatalysis at oxide electrodes. Concerted electron-proton transfer. *Inorg Chem* 50:2076–2078.
13. Miyazaki S, Kojima T, Mayer JM, Fukuzumi S (2009) Proton-coupled electron transfer of ruthenium(III)-pterin complexes: A mechanistic insight. *J Am Chem Soc* 131:11615–11624.
14. Alligrant TM, Alvarez JC (2011) The role of intermolecular hydrogen bonding and proton transfer in proton-coupled electron transfer. *J Phys Chem C Nanomater Interfaces* 115:10797–10805.
15. Zhang WB, Rosendahl SM, Burgess IJ (2010) Coupled electron/proton transfer studies of benzoquinone-modified monolayers. *J Phys Chem C Nanomater Interfaces* 114:2738–2745.
16. Reece SY, Nocera DG (2009) Proton-coupled electron transfer in biology: Results from synergistic studies in natural and model systems. *Annu Rev Biochem* 78:673–699.
17. Meyer TJ, Huynh MHV, Thorp HH (2007) The possible role of proton-coupled electron transfer (PCET) in water oxidation by photosystem II. *Angew Chem Int Ed Engl* 46:5284–5304.
18. Chen ZF, Concepcion JJ, Jurss JW, Meyer TJ (2009) Single-site, catalytic water oxidation on oxide surfaces. *J Am Chem Soc* 131:15580–15581.
19. Chen ZF, et al. (2010) Concerted O atom-proton transfer in the O-O bond forming step in water oxidation. *Proc Natl Acad Sci USA* 107:7225–7229.
20. Concepcion JJ, Jurss JW, Templeton JL, Meyer TJ (2008) One site is enough. Catalytic water oxidation by $[Ru(tpy)(bpm)(OH_2)]^{2+}$ and $[Ru(tpy)(bpz)(OH_2)]^{2+}$. *J Am Chem Soc* 130:16462–16463.
21. Concepcion JJ, et al. (2009) Making oxygen with ruthenium complexes. *Acc Chem Res* 42:1954–1965.
22. McDaniel ND, Coughlin FJ, Tinker LL, Bernhard S (2008) Cyclometalated iridium(III) aquo complexes: Efficient and tunable catalysts for the homogeneous oxidation of water. *J Am Chem Soc* 130:210–217.
23. Hull JF, et al. (2009) Highly active and robust Cp* iridium complexes for catalytic water oxidation. *J Am Chem Soc* 131:8730–8731.
24. Wasylenko DJ, et al. (2010) Electronic modification of the $[Ru^{II}(tpy)(bpy)(OH_2)]^{2+}$ scaffold: Effects on catalytic water oxidation. *J Am Chem Soc* 132:16094–16106.
25. Paul A, et al. (2011) Multiple pathways for benzyl alcohol oxidation by $Ru^{V}{=}O^{3+}$ and $Ru^{IV}{=}O^{2+}$. *Inorg Chem* 50:1167–1169.
26. Thompson MS, Meyer TJ (1982) Mechanisms of oxidation of 2-propanol by polypyridyl complexes of ruthenium(III) and ruthenium(IV). *J Am Chem Soc* 104:4106–4115.
27. Bard AJ, Faulkner LR (2001) *Electrochemical Methods: Fundamentals and Applications* (Wiley, New York), 2nd Ed,, pp 580–631.
28. Trammell SA, Meyer TJ (1999) Diffusional mediation of surface electron transfer on TiO_2. *J Phys Chem B* 103:104–107.
29. Bratsch SG (1989) Standard electrode potentials and temperature coefficients in water at 298.15 K. *J Phys Chem Ref Data* 18:1–21.
30. Auer B, Fernandez LE, Hammes-Schiffer S (2011) Theoretical analysis of proton relays in electrochemical proton-coupled electron transfer. *J Am Chem Soc* 133:8282–8292.
31. Chen ZF, et al. (2010) Nonaqueous catalytic water oxidation. *J Am Chem Soc* 132:17670–17673.
32. Brennaman MK, et al. (2011) Interfacial electron transfer dynamics following laser flash photolysis of $[Ru(bpy)_2((4,4'\text{-}PO_3H_2)_2bpy)]^{2+}$ in TiO_2 nanoparticle films in aqueous environments. *ChemSusChem* 4:216–227.
33. Muzikar J, van de Goor T, Gaš B, Kenndler E (2002) Propylene carbonate as a nonaqueous solvent for capillary electrophoresis: Mobility and ionization constant of aliphatic amines. *Anal Chem* 74:428–433.
34. Hoertz PG, Chen ZF, Kent CA, Meyer TJ (2010) Application of high surface area tin-doped indium oxide nanoparticle films as transparent conducting electrodes. *Inorg Chem* 49:8179–8181.
35. Chen ZF, Concepcion JJ, Hull JF, Hoertz PG, Meyer TJ (2010) Catalytic water oxidation on derivatized nanoITO. *Dalton Trans* 39:6950–6952.
36. Concepcion JJ, et al. (2010) Catalytic water oxidation by single-site ruthenium catalysts. *Inorg Chem* 49:1277–1279.
37. Heimer TA, D'Arcangelis ST, Farzad F, Stipkala JM, Meyer GJ (1996) An acetylacetonate-based semiconductor-sensitizer linkage. *Inorg Chem* 35:5319–5324.